IEEE Access
Multidisciplinary | Rapid Review | Open Access Journal

Received September 7, 2020, accepted October 12, 2020, date of publication October 23, 2020, date of current version November 6, 2020.

Digital Object Identifier 10.1109/ACCESS.2020.3033480

Automatic Classifying of Patients With Non-Traumatic Fractures Based on Ultrasonic Guided Wave Spectrum Image Using a Dynamic Support Vector Machine

JEAN-GABRIEL MINONZIO[1,2], BRYAN CATALDO[4], RODRIGO OLIVARES[1], (Member, IEEE), DONATIEN RAMIANDRISOA[3], RICARDO SOTO[4], BRODERICK CRAWFORD[4], (Member, IEEE), VICTOR HUGO C. DE ALBUQUERQUE[5,6], (Senior Member, IEEE), AND ROBERTO MUNOZ[1], (Member, IEEE)

[1]Escuela de Ingeniería Informática, Universidad de Valparaíso, Valparaíso 2362735, Chile
[2]Centro de Investigación y Desarrollo en Ingeniería en Salud, Universidad de Valparaíso, Valparaíso 2362735, Chile
[3]Bleu Solid, 77400 Pomponne, France
[4]Escuela de Ingeniería Informática, Pontificia Universidad Católica de Valparaíso, Valparaíso 2362807, Chile
[5]Department of Computer Science, Federal Institute of Education, Science and Technology of Ceará, Fortaleza CE 60040-215, Brazil
[6]Department of Teleinformatics Engineering, Federal University of Ceará, Fortaleza CE 60020-181, Brazil

Corresponding author: Roberto Munoz (roberto.munoz@uv.cl)

The work of Jean-Gabriel Minonzio, Rodrigo Olivares, and Roberto Munoz was supported by Grant CONICYT / FONDECYT / REGULAR / 1201311. The work of Ricardo Soto was supported by Grant CONICYT / FONDECYT / REGULAR / 1190129. The work of Broderick Crawford was supported by Grant CONICYT / FONDECYT / REGULAR / 1171243. The work of Victor Hugo C. de Albuquerque was supported by the Brazilian National Council for Research and Development (CNPq) under Grant 304315/2017-6 and Grant 430274/2018-1.

ABSTRACT Bone fractures are caused by diseases or accidents and are a widespread problem throughout the globe. Worldwide, 1.6 millions of hip fractures occur every year and are expected to rise to 6.3 millions in 2050. The current gold standard to assess fracture risk is the Dual-energy X-ray Absorptiometry (DXA), which provides a projected image of the bone from which areal bone mineral density is extracted. Ultrasound techniques have been proposed as non invasive alternatives. Recently, estimates of cortical thickness and porosity, obtained by Bi-Directional Axial Transmission (BDAT) in a pilot clinical study, have been shown to be associated with non-traumatic fractures in post menopausal women. Cortical parameters were derived from the comparison between experimental and theoretical guided modes. This model-based inverse approach failed for the patients associated with poor guided mode information. Moreover, even if the fracture discrimination ability was found similar to DXA, it remained moderate. The goal of this paper is to explore if these two limitations could be overcome by using automatic classification tools, independent of any waveguide model. To this end, a dynamic machine learning approach based on a Support Vector Machine (SVM) has been used to classify ultrasonic guided wave spectrum images measured by BDAT on post menopausal women with or without non-traumatic fractures. This approach has then been improved using parameters tuned by Bat Algorithm Optimization (BOA). The applied methodology focused on the extraction of texture features through a gray level co-occurrence matrix, structural comparison and histograms. The results accuracy was assessed using a confusion matrix. The effectiveness of the learning approach reached an accuracy of 92.31%.

INDEX TERMS Cortical bone, osteoporosis, fracture discrimination, quantitative ultrasound, guided waves, support vector machine, bat algorithm, guided wave spectrum image.

I. INTRODUCTION

Bone fractures are a widespread problem around the world, 1.6 millions of hip fractures occur every year worldwide and are expected to rise to 6.3 millions in 2050 [1]. In addition,

The associate editor coordinating the review of this manuscript and approving it for publication was Paolo Napoletano.

1 in 3 women and 1 in 5 men over 50 years old are expected to suffer an osteoporotic fracture [2]. In the case of Latin America, the projections from 1990 to 2050 suggest that the number of hip fractures for both men and women between 50-64 years old is expected to increase up to 400%; while for the elderly over 65 year old, this number is expected to increase to 700% [3].

The current gold standard to assess fracture risk is the Dual-energy X-ray Absorptiometry (DXA), providing areal Bone Mineral Density (aBMD in $g.cm^{-2}$) as well as its normalized and adimensional counterpart T-score [4]. Indeed, osteoporosis in adults is diagnosed based on a T-score, equal to or below -2.5. However, most individuals who sustain fragility fractures are above this arbitrary cutoff [5], [6]. Due to its projective nature, this technique provides little information about the composition and the 3D-geometric properties determining bone strength. The context of this work is the development of novel medical devices aiming to complement the current gold standard for bone status assessment, i.e., DXA.

Several alternative X-Rays techniques provide 3D images, from which it is possible to extract material and geometrical properties such as Cortical Thickness (Ct.Th) and volumetric Bone Mineral Density (vBMD in $g.cm^{-3}$). Those parameters can be directly measured at the main fracture sites (hip and spine), using Quantitative Computed Tomography (QCT) [7], while peripheral-QCT (pQCT) [8] and High-Resolution pQCT (HR-pQCT) [9] are restricted to peripheral sites (forearm and tibia). HR-pQCT provides a spatial resolution, about 50 mum, better than QCT and pQCT resolutions, about a millimeter, but its large volume and cost limit a wide use. Image processing techniques, like StrAx1.0 software for QCT, propose to obtain cortical porosity (Ct.Po) estimates from gray level of both central QCT [7] and HR-pQCT [10]. Similarly, bone porosity index derived from Magnetic resonance imaging (MRI) has been found correlated to mechanical stiffness [11].

Ultrasound techniques, sensitive to both geometrical and elastic properties of bone, have been proposed as non invasive, affordable and portable alternatives [12]. They can be divided among three main approaches. A first approach is based on the measurement of heuristic parameters, such as Broadband Ultrasonic Attenuation (BUA in $dB.MHz^{-1}.cm^{-1}$), [13] velocities (in $m.s^{-1}$) of the First Arriving Signal [14]–[16] or of the Fundamental Flexural Guided Wave [17]. A second approach proposes to provide aBMD surrogates, combining different ultrasonic parameters and eventually additional clinical data, at the hip and spine [18] as well as forearm and lower leg [19]. Finally, a third approach, based on inverse problem schemes, aims to provide intrinsic bone properties potentially conveying information beyond aBMD [20].

A first difficulty of inverse problems is the number of parameters or unknowns to be estimated. For example, in the case of a 2D transverse isotropic free plate waveguide, the number of parameters was reduced from 6, i.e., Ct.Th, the mass density and 4 stiffness coefficients C_{ij}, to 5, i.e., Ct.Th and 4 parameters being a shear velocity and 3 stiffness ratios [21]. Later, the number of parameter was reduced to 2, Ct.Th and Ct.Po, using a homogenization model providing the C_{ij} in function of porosity, assuming a universal bone matrix [22]. Different inverse problem approaches have been explored, based on for example gradient method [21], genetic algorithm [23] or the projection of the theoretical modes onto the singular vectors basis [24], the latter allowing to avoid the labeling step of the experimental modes. Theses approaches are usually efficient if the number of measurable modes is not too large, i.e., if the wavelengths are larger than the cortical thickness ranging typically from 1 to 5 mm. At high ultrasonic frequencies (more than 3 MHz), wavelengths are smaller than the cortical thickness and ray path model is more adapted [25]. Despite viscoelastic absorption, this point of view has been recently proposed using a ray-tracing technique in two imaging planes (along and perpendicular to the bone axis) [26] and in multifocus pulse-echo [27].

Recently, estimates of Ct.Th and Ct.Po, derived from guided wave spectrum measured by bi-directional axial transmission (BDAT), have been tested in a pilot clinical study [28]. In this, study, Ct.Po discrimination between fractured and non-fractured patients, was found similar to DXA, with an AUC, Area Under the Receiver Operator Characteristic (ROC) Curve, equal to 71%, after adjustement performed according to age, Body Mass Index (BMI) and cortisone treatment. Indeed, the success of an inverse problem, i.e., its ability to deliver a robust and non ambiguous solution, depends on the measurement quality and the ability of the model to represent realistic cortical bone layer. In particular, some BDAT measurement failures have been associated with large soft tissue thickness [28] or irregular inner interface [29]. Thus, the objective of this study is to explore if those two limitations of the BDAT approach, moderate failure rate and fracture discrimination similar to DXA, could be overcome by automatic classification tools.

Accurate processing of medical images is indeed crucial for everyday detection or classification of diseases. This area is in constant development especially due to the improvement in recognition techniques. For example, the Support Vector Machine (SVM) approach, widely used in image classification, was first presented by Cortes and Vapnik in 1995 [30]. An other typical case is the exponential development and use of deep learning for Magnetic Resonance Imaging (MRI) image processing since 2009 [31]. Deep learning has been applied to image acquisition and segmentation as well as diagnosis and prognosis [31], thus evidencing that it is possible to get high accuracy in classification of medical images. For example, Convolutional Neural Networks (CNN) were used for the diagnosis of brain tumors with a two-phase model, achieving an accuracy of 99.55% from a database of 349 MRI images [32]. Likewise, Gray Level Concurrency Matrix (GLCM) features was used in analysis of cancer cells using laser pico-projections images [33] or in detection of bone fractures in X-ray images [34]. Similarly, deep learning

with CNN [35], application of K-Nearest Neighbors algorithm (KNN) to decision trees [36] have been applied for the analysis of X-ray image in order to detect and characterize bone fractures. Similar approaches have also been tested in ultrasonic echography. For example, automatic classification of pediatric pneumonia, based on pattern recognition in ultrasonic images of lungs, has been proposed in 2018 through a neural network, identifying pneumonia with a 90.9% sensitivity and 100% specificity [37]. Analogous developments have recently been proposed for automatic bone surface segmentation in ultrasonic echographic images [38]–[40]. These image processing systems play an important role for the automatic detection and are expected to support professionals in making diagnosis.

Machine learning techniques have recently been applied in the context of ultrasound characterization of bone. Using a SVM, *ex vivo* rabbit bones with different levels of demineralization, were classified using a velocity extracted from the acoustic pressure, with an accuracy greater than 80% [41]. Similarly, using low frequency (3kHz) flexural guided waves and a SVM on 41 patients, a distinction was made between healthy and osteoporotic patients with an accuracy of 56% for the spine, 83% for the radius, and 71% for the hip [42]. In a recent simulation study, an artificial neural network has been proposed to estimate micro-architectural properties of cortical bone using ultrasonic attenuation [43]. Likewise, a CNN has been tested to estimate CT.Th and bulk velocities using simulated ultrasonic guided waves [44]. In addition, similar machine learning-based approaches have also been recently introduced in non destructive testing in case of guided wave damage detection [45] or localization and characterization [46].

Thus in this paper, automatic classification tools have been tested on the same clinical data set of guided wave spectrum images obtained by BDAT in a previous cross-sectional study [28]. To achieve our aim, we build a dynamic SVM model that allows us to classify non-fractured patients and patients who suffered non-traumatic fractures. This model uses a self-adaptive approach in order to find the best parameter values of the SVM, given by the Bat Algorithm Optimization (BOA) metaheuristic [47]. The document presented is organized as follows. Section II presents the instrumentation and data. Sections III and IV explain in detail the methodology used to address this work. Finally, classification results and the discussion of this study are presented in Sections V and VI, respectively.

II. INSTRUMENTATION AND DATA

Ultrasonic measurements were carried out with a 1-MHz BDAT prototype (Azalée, Paris, France), adapted to forearm measurement. The experimental setup and device, with the probe placed at the one-third distal radius, are shown on Figure 1. The probe was specifically designed to measure the propagation of guided waves in two directions in order to correct the biases induced by the inclination angle between the probe and the bone, due to the overlaying soft

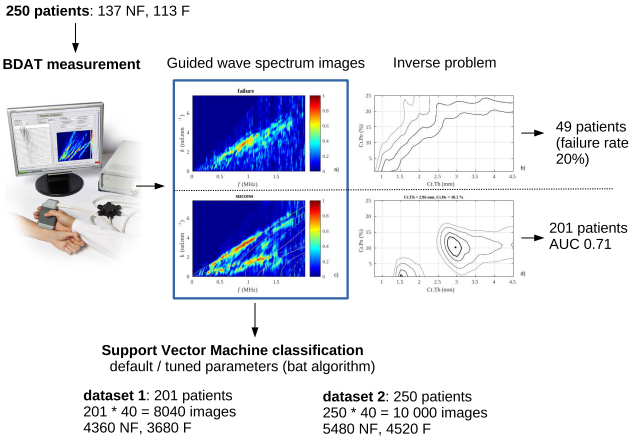

FIGURE 1. General purpose of the paper: Guided wave spectrum images obtained in [28] in 201 post menopausal women with (F) or without (NF) non-traumatic fractures are analysed with Support Vector Machine (SVM) with parameters tuned using the Bat Algorithm Optimization (BOA). A second dataset of 250 patients, including the 49 failure cases of the inverse problem approach, is also tested.

tissues [48]. In the following, direction 1 corresponds to the distal wave propagation direction, i.e., from elbow to wrist, while the opposite proximal direction is denoted direction 2. For both directions, guided wave spectrum images were obtained using a specific signal processing, applied to the multiple transmitter - multiple receiver probe, the so-called SVD-based method, where the acronym SVD stands for Singular Value Decomposition [49]. Guided wave spectrum images, denoted by $Norm(f, k)$, expressed in the frequency f - wavenumber k domain, can be interpreted as enhanced spatio-temporal Fourier transforms. Each pixel (f, k) of the *Norm* function is defined by the norm of a normalized attenuated plane wave projected onto the basis of the receiver singular vectors [50]. The pixel value reflects in a $0-1$ scale the presence rate of the tested plane wave in the measured signals. This procedure generated the guided wave spectrum images to be classified in this work. It can be noted that this approach was then extended to an inverse procedure providing estimates of two cortical parameters: Ct.Th and Ct.Po [29]. Inverse problem results obtained in [28] will be used as a baseline in the following.

A dedicated human-machine interface (BleuSolid, Pompone, France) was developed to show guided wave spectrum in quasi-real time. This interface was meant to guide the operator in finding a correct probe position with respect to the main bone axis. A complete measurement consisted of multiple series of 20 acquisitions of two guided wave spectrum images, one per direction. Each series corresponded to a probe repositioning. Two typical examples of guided wave spectrum images are shown in Figure 1 corresponding to failure or success cases of the inverse procedure providing estimates of Ct.Th and Ct.Po [28]. It can be observed that the first image is associated with ''blurred'' modes, while in the second one, modes appear clearer and are in agreement with the modes of the optimal guided wave model, shown with lines in Figure 1.

The guided wave spectrum images were obtained on 301 postmenopausal patients recruited in the rheumatology department of the Cochin hospital (Paris, France). This cross-sectional study has been approved by the ethical committee Ile de France III. A written informed consent was provided by the patients. The procedure of the study was in accordance with the Declaration of Helsinki. Exclusion criteria were: missing data ($n = 7$), patient suffering from a cancer ($n = 1$), two hip replacement (no femoral DXA possible, $n = 9$), BMI < 15 ($n = 1$), a history of traumatic fractures ($n = 33$). Thus, a total of 51 patients out of 301 were excluded. In addition, 49 patients were associated with failure of the ultrasonic inverse problem. Finally, a total of 201 patients constituted the initially studied data set, denoted dataset 1 in the following.

Two groups were considered, a control group with patients without fracture (NF, $n = 109$) and a fractured group of patients with any non-traumatic fracture (F, $n = 92$). Fracture sites were hip, wrist, spine, humerus, tibia, ankle, and rib. Details about the types and number of non-traumatic fractures can be found in [28]. As the number of repositioning varied from 1 to 6, it was decided to take, in a paired way, 20 random images, 10 per direction, for each patient. Thus, with a final data set of 201 patients, a total of $201 \times 40 = 8{,}040$ images was formed, i.e., 4,020 per direction.

One of the main advantages of the machine learning approach is the possibility to analyse all guided wave spectrum images, even in case of inverse problem failure. Thus, a second set, denoted dataset 2, of 250 patients (10,000 images) was also considered, corresponding to the 201 previous patients plus the 49 failure cases. The number of patients in each group are respectively equal to 137 (NF) and 113 (F). For both datasets, i.e., 201 and 250 patients, results obtained with the machine learning approach will be compared to discrimination results obtained with the current gold standard DXA.

III. EXTRACTION OF THE FEATURE VECTOR

To achieve the classification of images between patients with or without non-traumatic fractures, four steps were followed: (1) Pre-processing step, (2) extraction of 8 features of the Structural SIMilarity index (SSIM) and the Mean Square Error (MSE), (3) extraction of 24 features of the Gray Level Concurrency Matrix (GLCM) and finally (4) generation of a vector with 32 features based on the results of the previous steps. The feature vector will be denoted **A** in the following. The extraction process of each feature will be explained in detail further in this section.

A. PRE-PROCESSING STEP

The aim of the pre-processing step is twofold: denoising and merging two guided wave spectrum images, associated with the two directions of the bi-directional measurement. The dimensions of each image are $Nf\ (=100) \times Nk\ (=75)$ pixels, later denoted by $m \times n$. As the pixel value ranges from 0 to 1, the denoising step is achieved by setting to zero all pixels lower than a threshold equal to 0.4. It should be noted that this threshold was selected through a sampling phase. As the two directions are not equivalent, the denoising step was sequentially applied to each direction as illustrated in Figure 2. Indeed, the wave propagation in the elbow-wrist direction (direction 1) is associated with longer and clearer modes in the guided wave spectrum image due to the fact that the cortical bone layer is thinner close to the bone extremities [51]. That is why, the denoising step is firstly applied to the guided wave spectrum image associated with direction 2. The resulting denoised image is then merged with the direction 1 image, by calculating the per-element bit-wise conjunction as: if one of the two pixels is zero then the resulting pixel is zero, otherwise the resulting pixel corresponds to the mean. Finally, a second denoising is applied to the image containing information from both directions.

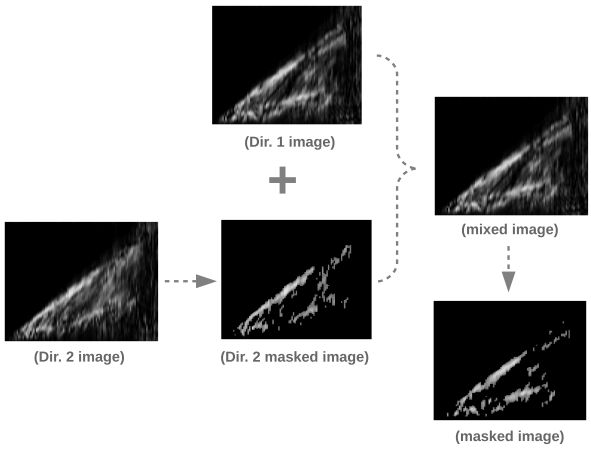

FIGURE 2. Illustration of the pre-processing step: the two guided wave spectrum images, associated with the two directions of the bi-directional measurement, are denoised and merged into a pre-processed image.

B. REGIONS OF INTEREST

The extraction of the feature vector **A** is based on the analysis of three regions of interest (ROI) of the guided wave spectrum image as illustrated on Figure III-B. The ROIs are separated by two linear functions, denoted LF1 and LF2 to whose equations are given by $k = 2\pi f/v$, with k the wavenumber (rad. mm^{-1}), f the frequency (MHz) and v the phase velocity, equal to 1.9 and 4 mm.$\mu\ s^{-1}$ for LF1 and LF2 respectively. The first ROI corresponds to the part of the image above LF1 while ROI3 corresponds to the part below LF2. Finally ROI2 corresponds to the part between the two linear functions. In step (2), SSIM and MSE, the comparaison of ROI1 and ROI3 to LF1 and LF2 leads to 8 features, while 24 features are extracted in step (3) GLCM, 8 in each ROI. Note that no information is taken into account for phase velocities lower than 1.4 mm.$\mu\ s^{-1}$, i.e., the zone above the dotted line. It can be observed that similar linear patterns appear in measured spectrum as shown in Figure III-B, associated respectively with the $A0$ mode and the longitudinal bulk wave velocity [52].

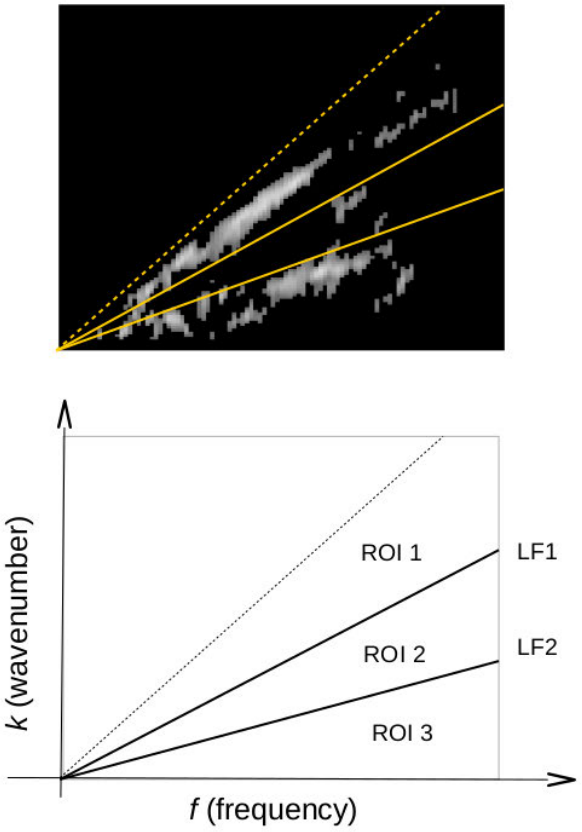

FIGURE 3. Example of pre-processed image with summary of the regions of interest (ROI) and reference lines used in the feature extraction process.

C. SSIM AND MSE

The second step, corresponding to the SSIM and MSE feature extraction, is based on the comparisons of ROI1 and 3 with reference images, associated with the two linear functions LF1 and 2. To do this, a Canny filter is applied to the pre-processed guided wave spectrum image, obtained from step (1), and later divided into ROI1 and 3. The idea behind the Canny filter is to obtain structural information about the image, in particular the mode positions, as this algorithm is designed to detect the edges providing the contour of the modes. Figure 4 shows how each ROI is contrasted with each linear function, leading to the four comparisons mentioned above: ROI1 compared with LF1 and LF2 as well as ROI3 compared with LF1 and LF2. From each comparison, two measurements, MSE and the SSIM are obtained, thus a total of 8 features is obtained from this process.

The first measurement, i.e., MSE, represents the difference in pixel intensities of an image

$$MSE = \frac{1}{mn}\sum_{i=1}^{m}\sum_{j=1}^{n}(I_{ij} - K_{ij})^2, \tag{1}$$

with ij the pixel position, m and n the image dimensions and I and K the two compared images, i.e., I being ROI1 or 3, and K being the LF 1 or 2 image.

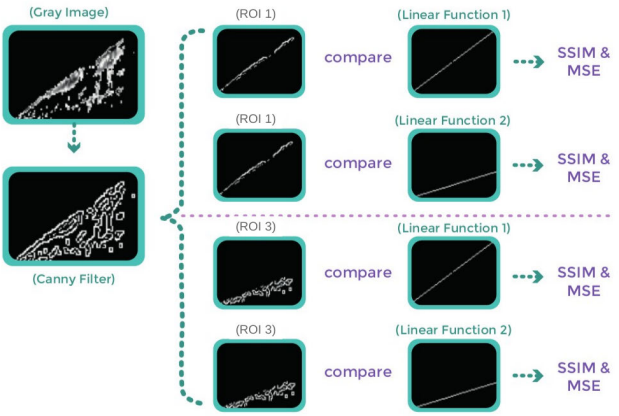

FIGURE 4. Image processing for extraction of SSIM and MSE features.

The second measurement, i.e., SSIM, represents the changes in the structural information allowing to determine the similarity between two images [53]

$$SSIM(I, K) = \frac{(2\mu_I\mu_K + c_1)(2\sigma_{IK} + c_2)}{(\mu_I^2 + \mu_K^2 + c_1)(\sigma_I^2 + \sigma_K^2 + c_2)}, \tag{2}$$

with μ corresponding to means, σ to variances and covariances, while c are variables to stabilize the division with weak denominator. The parameters c_1 and c_2 were calculated as $(K_1L)^2$ and $(K_2L)^2$, where L corresponds to the dynamic range of pixels, i.e., 255 in the case of grayscale images, and with K_1 and K_2 being constants small compared to 1. Following [53], the values of K_1 and K_2 were chosen equal to 0.01 and 0.03, respectively.

D. GLCM

The second stage of features extraction corresponds to GLCM. For each ROI, 8 features are calculated, from which the two first are linked with graphic information while the other six are associated with relationships between pixels. The first two measures, mean and standard deviation, are generated from a histogram of the pixel gray level value. The other six measures are extracted from the Gray Level Concurrency Matrix: energy, dissimilarity, contrast, homogeneity, correlation and angular second moment.

The Angular Second Moment (ASM) corresponds to the sum of the square elements P_{ij} of the image. The energy, also known as uniformity, corresponds to the square root of ASM. The correlation corresponds to a measure of relationship or dependence between a pixel and its neighbor in the whole image. Dissimilarity is a measure of local variation of intensity defined as the average absolute difference between pairs of neighboring pixels. The contrast, also called inertia, illustrates the difference in intensity between a pixel and its neighbor over the entire image. Finally, the homogeneity represents the proximity of the distribution of elements in the GLCM with its diagonal. These features are defined in equations 3 to 8 as in [54].

$$ASM = \sum_{i=1}^{m}\sum_{j=1}^{n}P_{ij}^2 \tag{3}$$

$$Energy = \sqrt{ASM} \tag{4}$$

$$Correlation = \sum_{i=1}^{m}\sum_{j=1}^{n} P_{ij}^2 \left[\frac{(i-\mu_i)(j-\mu_j)}{\sigma_i\sigma_j}\right] \tag{5}$$

$$Dissimilarity = \sum_{i=1}^{m}\sum_{j=1}^{n} P_{ij}|i-j| \tag{6}$$

$$Contrast = \sum_{i=1}^{m}\sum_{j=1}^{n} P_{ij}(i-j)^2 \tag{7}$$

$$Homogeneity = \sum_{i=1}^{m}\sum_{j=1}^{n} \left[\frac{P_{ij}}{1+(i-j)^2}\right] \tag{8}$$

This extraction process, i.e., step (3), is repeated for each ROI, which results in a total of 24 values, and together with those 8 mentioned in step (2), generate the vector **A** of 32 features.

IV. CLASSIFICATION

Classification is performed using the vector **A** of 32 features, using 80% of the samples as training and 20% as tests. The classification is done 20 times. The number of classification repetitions (i.e., 20) was selected equal to the number of acquisitions per patients. From this, the training process of the classifier is performed where a support vector machine with a radial base function was selected as:

$$K(\mathbf{A}, \mathbf{A}') = exp\left(-\gamma||\mathbf{A}-\mathbf{A}'||^2\right) \tag{9}$$

with the difference between two feature vectors ‖**A** - **A**'‖ representing the Euclidean distance. The SVM has two parameters that can be adjusted, γ and C gathered into a single vector denoted $\bar{x}$ in Algorithm 1. The first parameter γ allows to control the curvature of the radial function, given by Eq. (9), while the second parameter C is used to control the error. Because the parameters must be adjusted for each problem, it was decided to opt for the automatic adjustment of these through a bio-inspired technique, in this case BOA. This algorithm was created by X.-S. Yang and the pseudo-code is depicted in Algorithm 1 [47]. In this case, the objective of the algorithm is to optimize (maximize) the accuracy achieved by the SVM which is represented in the pseudo-code by the function $f(\bar{x})$.

Following Algorithm 1, each iteration or bat generation is associated with an SVM classifier. This classifier is built in the main loop statement that run while a stop criteria is not met. During this procedure, a model is validated by using a repeated cross-validation procedure which requires two phases for iteration. Each iteration uses five folds: four folds was applied in the training phase (80% of the image dataset), and one fold was employed in the testing phase (20% of the image dataset).

Bat optimizer tunes the SVM input parameters (C and γ). This method is able to to maximize the accuracy of the machine learning algorithm during the learning phase, iteratively. BOA provides agents or individuals (bats) capable of finding the sensitivity and specificity values and pass them to the SVM. Next, the SVM classifies the image and returns its accuracy. BOA takes this value as fitness (profit) and it checks if the new value is better than the best old value, then they are exchanged. Otherwise, values remain. Finally, the last

Algorithm 1 Bat Algorithm Optimization

Data: Population size *popSize*, minimum frequency f_{min}, maximum frequency f_{max}, and maximum number of iterations T.
Result: The best solution $\hat{x}$: a vector set with optimized γ and C values.

```
// Objective function.
// d is dimension of the problem.
f(x̄), x̄ = (x_1, x_2, ..., x_n)^d;
// Initialize: velocity, position, pulse rate, and loudness.
for bat i, (∀i = 1, ..., popSize) do
    for dimension j, (∀j = 1, ..., d) do
        v_i^j ← Random[0, 1];
        x_i^j ← Random[0, 1];
    end
    r_i ← Random[0, 1];
    A_i ← Random[0, 1];
end
// Produce T-generations of popSize bats.
while t < T do
    // Generate new solutions by adjusting frequency, and updating velocities and locations/solutions:
    for bat i, (∀i = 1, ..., popSize) do
        β ← Random[0, 1];
        f_i ← f_min + (f_max − f_min)β;
        for variable j, (∀j = 1, ..., d) do
            v_i^j ← v_i^j + [x̂^j − x_i^j]f_i;
            x_i^j ← v_i^j + x_i^j;
        end
    end
    // Randomly generate a local solution, x_new around the best solution.
    if Random[0, 1] > r_i then
        for variable j, (∀j = 1, ..., d) do
            x_new^j ← x_old^j + εĀ^t;
        end
        // Loudness average Ā governs the intensification process according to the echolocation phenom. This value is iteratively computed during the run (t-th generation). To control x_new^j takes bounded values, a ad-hoc constant ε is randomly generated in [−1, 1].
    end
    // Evaluate the new solution f(x_new)
    if Random[0, 1] < A_i and f(x_new) > f(x_i) then
        // Accept the new solution.
        // Increase r_i.
        r_i ← r_i^0[1 − e^(−γt)];
        // Reduce A_i.
        A_i ← αA_i;
    end
end
```

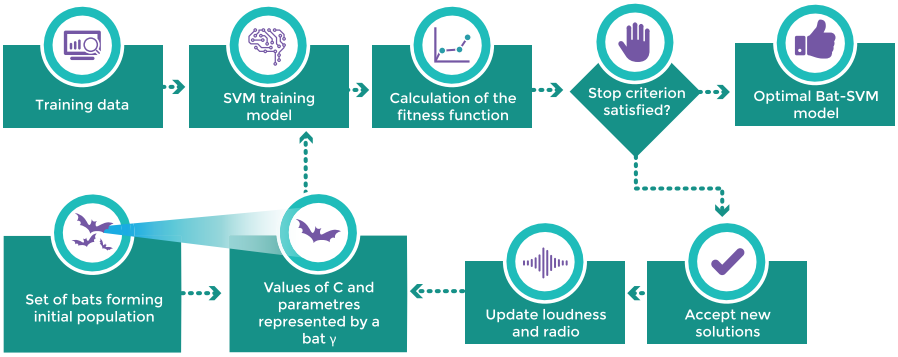

FIGURE 5. Training and adjustment of γ and C parameter values for SVM with Bat Algorithm Optimization.

iteration gives the best accuracy. After the complete execution of the metaheuristic, a trained model with the best adjustment for γ and C is obtained.

The complete process is shown graphically in Figure 5. The range of possible values were chosen equal to $[0.03 - 4]$ and $[4 - 10]$ for γ and C, respectively. The lower and upper limits were determined following the standard SVM scikit-learn[1] implementation, and are considered as the SVM default parameters. Results are analyzed in terms of accuracy and confusion matrix, in order to quantify false positives and false negatives due to their importance in a clinical context. Finally, we provide a statistical test for the comparison of the models with and without parameter tuning, in order to check if the parameter tuning is associated with a significant improvement.

For the pre-processing phase, the learning phase, and the classifying phase, Python v3.73 is used. Computational experiments were run on an Intel Core i3 1.9GHz machine with 4GB RAM and an NVIDIA GeForce 820M integrated card. Default configuration of the Anaconda Distribution is used. Referring to the libraries: we import OpenCV as main tool to implement the pre-processing phase of the images; Matplotlib was used for the data visual representation; for array manipulation we include Numpy library; finally, for mathematical operations Math library was used. For the feature extraction phase, skimage and scipy were used. At the end, the SVM standard model with the Cross-Validation and metrics were retrieve from the scikit-learn library.[2]

The ability of the different features to discriminate between the fractured and the non fractured groups, was also analysed using a reference method: the binomial logistic regression. Odds Ratios (ORs) were expressed as increases in the estimated fracture risk per one standard deviation decrease. To estimate the sensitivity and specificity of the different parameters for the fracture discrimination, the ROC curves were calculated and the AUC were determined. Adjusted ORs and AUCs were computed with age, BMI and cortisone as covariates. OR and AUCs were calculated using averaged (over the 20 images) feature values, i.e., 32 averaged features per patients.

[1]https://scikit-learn.org/stable/

[2]For further detail in the proposed approach and its replicability, we done available in https://github.com/Rainvert/Clasificacion-de-Imagenes-BDAT-Fracturas

V. RESULTS

A. LOGISTIC REGRESSION

Results of the binomial logistic regression analysis are given in Table 1 for the first dataset (201 patients) and Table 2 for the second dataset (250 patients). Only significant and marginal results, i.e., associated with p-value lower than 0.05 and 0.10 respectively, are reported. For the first dataset, unadjusted AUC values range from 0.58 to 0.63 while unadjusted OR range from 1.3 to 1.5, similar to Ct.Th or Ct.Po (AUC = 0.62, OR = 1.5) and lower than aBMD neck (AUC = 0.65, OR = 1.9). When adjusted, AUC and OR values were equal to 0.71 and about 1.4 respectively for both automatic features and Ct.Po, similar to aBMD neck values (AUC = 0.72, OR = 1.5). For the second dataset including failure cases of the inverse problem, unadjusted AUC values range from 0.57 to 0.60 while unadjusted OR range from 1.3 to 1.5 lower than aBMD neck (AUC = 0.68, OR = 2). When adjusted, AUC and OR values were equal to 0.75 and about 1.4 respectively, lower than aBMD neck values (AUC = 0.76, OR = 1.6).

B. SVM

The main objective of this study is to obtain a classifier based on a SVM that presents the best accuracy metric. Because SVM requires parameters for its classification, it is sought to obtain the best result by making an automatic selection of parameters. This is done through the application of a population metaheuristic, such as the BOA. From this process, the following results shown in Table 3 were obtained in 20 generations of 10 bats; the data are summarized every five generations. Furthermore, it indicates the minimum and maximum accuracy reached in each generation, throughout the process.

According to the computed results, one can observe that a high accuracy is already obtained in the first generation and this value remains equal or improves over the iterations. The algorithm quickly, in a reduced number of generations,

TABLE 1. Dataset 1 (201 patients): Odds ratios (OR) and areas under the ROC curve. AUC and OR are adjusted for age, BMI and cortisone. *p-value < 0.05. **p-value < 0.01. ***p-value < 0.001.

			unadjusted			adjusted		
			AUC [95% CI]	OR [95% CI]	p	AUC [95% CI]	OR [95% CI]	p
		Ct.Th	0.63 [0.56 - 0.71]	1.46 [1.09 - 1.94]**	0.008	0.70 [0.62 - 0.77]	1.18 [0.85 - 1.63]	0.310
		Ct.Po	0.62 [0.55 - 0.69]	1.47 [1.12 - 1.95]**	0.005	0.71 [0.60 - 0.77]	1.39 [1.02 - 1.89]*	0.035
		aBMD neck	0.65 [0.56 - 0.72]	1.88 [1.32 - 2.66]***	3.2e-04	0.72 [0.64 - 0.78]	1.48 [1.00 - 2.20]*	0.046
		aBMD femur	0.61 [0.52 - 0.68]	1.59 [1.15 - 2.19]**	0.004	0.71 [0.62 - 0.77]	1.25 [0.85 - 1.83]	0.242
SSIM	ROI 1	LF1						
	ROI 1	LF2	0.63 [0.58 - 0.70]	1.42 [1.05 - 1.91]*	0.020			
MSE	ROI 1	LF1	0.58 [0.52 - 0.61]	1.36 [1.01 - 1.82]*	0.036			
	ROI 1	LF2	0.61 [0.52 - 0.71]	1.42 [1.06 - 1.90]*	0.016			
	ROI 3	LF1				0.71 [0.66 - 0.77]	1.42 [1.02 - 1.97]*	0.033
	ROI 3	LF2				0.71 [0.66 - 0.74]	1.44 [1.03 - 2.02]*	0.031
GLCM	ROI 1	Histogram SD	0.60 [0.57 - 0.65]	1.44 [1.06 - 1.96]*	0.018			
		Dissimilarity	0.62 [0.57 - 0.69]	1.47 [1.09 - 1.98]**	0.010			
		Contrast	0.59 [0.54 - 0.62]	1.32 [1.00 - 1.75]*	0.045			
		Homogeneity	0.60 [0.50 - 0.68]	1.46 [1.07 - 2.00]*	0.014			
		ASM	0.60 [0.56 - 0.65]	1.45 [1.07 - 1.98]*	0.016			
		Energy	0.60 [0.53 - 0.69]	1.45 [1.07 - 1.98]*	0.016			
		Correlation	0.57 [0.52 - 0.65]	1.34 [0.99 - 1.81]	0.053			
GLCM	ROI 2	Correlation	0.58 [0.54 - 0.62]	1.33 [1.02 - 1.73]*	0.030			
GLCM	ROI 3	Histogram SD				0.71 [0.63 - 0.83]	1.36 [0.98 - 1.88]	0.063
		Dissimilarity				0.71 [0.61 - 0.75]	1.36 [0.99 - 1.86]	0.053
		Contrast				0.71 [0.65 - 0.74]	1.32 [0.97 - 1.80]	0.073
		Homogeneity				0.71 [0.65 - 0.78]	1.37 [0.99 - 1.89]	0.054
		ASM				0.71 [0.69 - 0.74]	1.37 [0.99 - 1.91]	0.052
		Energy				0.71 [0.65 - 0.75]	1.37 [0.99 - 1.89]	0.056
		Correlation				0.71 [0.67 - 0.76]	1.36 [0.96 - 1.92]	0.079

TABLE 2. Dataset 2 (250 patients): Odds ratios (OR) and areas under the ROC curve. AUC and OR are adjusted for age, BMI and cortisone. *p-value < 0.05. **p-value < 0.01. ***p-value < 0.001.

			unadjusted			adjusted		
			AUC [95% CI]	OR [95% CI]	p	AUC [95% CI]	OR [95% CI]	p
		Ct.Th	x	x		x	x	
		Ct.Po	x	x		x	x	
		aBMD neck	0.68 [0.62 - 0.75]	2.06 [1.50 - 2.82]***	4.6e-06	0.76 [0.68 - 0.80]	1.57 [1.09 - 2.26]*	0.014
		aBMD femur	0.64 [0.57 - 0.71]	1.73 [1.30 - 2.31]***	1.3e-04	0.75 [0.69 - 0.82]	1.37 [0.96 - 1.94]	0.075
SSIM	ROI 1	LF1	0.56 [0.49 - 0.61]	1.33 [1.00 - 1.76]*	0.043			
	ROI 1	LF2	0.61 [0.58 - 0.67]	1.43 [1.08 - 1.90]*	0.011			
MSE	ROI 1	LF1	0.58 [0.54 - 0.64]	1.46 [1.10 - 1.93]**	0.007			
	ROI 1	LF2	0.58 [0.54 - 0.64]	1.46 [1.10 - 1.93]**	0.007			
	ROI 3	LF1				0.75 [0.69 - 0.81]	1.40 [1.03 - 1.89]*	0.028
	ROI 3	LF2				0.74 [0.65 - 0.82]	1.40 [1.03 - 1.91]*	0.028
GLCM	ROI 1	Histogram SD	0.60 [0.56 - 0.62]	1.47 [1.11 - 1.95]**	0.007			
		Dissimilarity	0.61 [0.55 - 0.70]	1.51 [1.13 - 2.02]**	0.004			
		Contrast	0.60 [0.55 - 0.66]	1.42 [1.07 - 1.89]*	0.013			
		Homogeneity	0.60 [0.58 - 0.67]	1.49 [1.12 - 1.98]**	0.005			
		ASM	0.60 [0.56 - 0.63]	1.48 [1.11 - 1.97]**	0.006			
		Energy	0.60 [0.54 - 0.65]	1.48 [1.11 - 1.97]**	0.006			
		Correlation	0.57 [0.52 - 0.62]	1.31 [1.00 - 1.71]*	0.045			
GLCM	ROI 2	Correlation	0.57 [0.52 - 0.62]	1.29 [1.02 - 1.63]*	0.030			
GLCM	ROI 3	Histogram SD				0.75 [0.70 - 0.77]	1.36 [1.01 - 1.84]*	0.041
		Dissimilarity				0.75 [0.67 - 0.79]	1.35 [1.01 - 1.82]*	0.041
		Contrast				0.74 [0.72 - 0.81]	1.32 [0.99 - 1.78]	0.056
		Homogeneity				0.75 [0.70 - 0.78]	1.37 [1.01 - 1.84]*	0.038
		ASM				0.75 [0.65 - 0.78]	1.37 [1.02 - 1.86]*	0.035
		Energy				0.75 [0.73 - 0.79]	1.37 [1.01 - 1.84]*	0.038
		Correlation				0.74 [0.69 - 0.79]	1.36 [0.99 - 1.87]	0.051

managed to converge to an acceptable adjustment of parameters. Each accuracy obtained corresponds to an average of the training validated with 5 folds and 2 iterations of repeated cross-validation. The automatic classification was also carried out using default parameters, i.e., γ and C equal to 0.031 and 1.0, respectively. Results obtained with the two

TABLE 3. Adjustment of SVM parameters with bat algorithm. ACC: Accuracy.

Dataset 1				
N°	Min ACC	Max ACC	γ	C
Gen 1	86.90%	92.23%	0.325	5.659
Gen 5	89.23%	92.30%	0.361	6.800
Gen 10	90.18%	92.30%	0.361	6.800
Gen 15	92.08%	92.30%	0.361	6.800
Gen 20	92.08%	92.31%	0.344	6.319
	Best Bat	92.31%	0.344	6.319
Dataset 2				
N°	Min ACC	Max ACC	γ	C
Gen 1	90.27%	91.76%	0.382	9.490
Gen 5	90.27%	91.78%	0.383	9.145
Gen 10	91.76%	91.84%	0.483	9.582
Gen 15	91.75%	91.84%	0.483	9.582
Gen 20	91.75%	91.85%	0.490	9.186
	Best Bat	91.85%	0.490	9.186

TABLE 4. Comparison of accuracy (ACC) provided by the unadjusted and BOA adjusted SVM models.

Dataset1	ACC	γ	C
SVM + Default parameters	74.34%	0.031	1.000
SVM + BOA	92.31%	0.344	6.319
Accuracy Improvement	17.97%		

Dataset2	ACC	γ	C
SVM + Default parameters	72.80%	0.031	1.000
SVM + BOA	91.85%	0.490	9.186
Accuracy Improvement	19.05%		

TABLE 5. Adjusted SVM average confusion matrix (SVM + BOA). F: Fractured - NF: Non Fractured.

Dataset 1	Predicted NF	Predicted F
Actual NF	50.97%	3.26%
Actual F	4.43%	41.34%
Dataset 2	NF	F
Actual NF	51.76%	3.04%
Actual F	5.11%	40.09%

methods, default and tuned parameters, are shown in Table 4. For both datasets, it can be observed that the accuracy greatly increased when the parameters γ and C were adjusted, from about 72-74% to about 91-92%.

In order to test if the adjustment of the γ and C parameters provided a significant improvement in comparison with the unadjusted case (Table 4), two statistical tests were applied to the distributions containing the 20 execution results [55]. The normality was assessed using a Kolmogorov-Smirnov-Lilliefors test leading to the use of the non-parametric test, Wilcoxon-Mann-Whitney. For both datasets, the BOA provided a significantly better accuracy, with a p value lower than 10^{-10}.

The training of an SVM model with adjusted γ and C parameters provided average accuracy of 92.31% (dataset 1) and 91.85% (dataset 2). The corresponding confusion matrices are shown in Table 5. Measures derived from the confusion matrix, i.e., precision, recall, F1-Score and specificity, are given in Table 6, with values ranging from 0.89 to 0.95.

TABLE 6. Measures from confusion matrix: Measure correspond to non-fractured class as positive (SVM + BOA).

	Dataset 1	**Dataset 2**
Precision	0.9399	0.9445
Recall	0.9201	0.9101
F1-Score	0.9299	0.9270
Specificity	0.9033	0.8869

As mentioned earlier, 20% of the data was used for testing, which corresponds to 804 and 1000 images for datasets 1 and 2 respectively. If the conversion is made per patient this equates to 40 and 50 patients, since each one has 20 images. Based on this, we compare how many of the 20 samples were correctly predicted by the model, obtaining with a percentage of certainty or closeness to the known diagnosis of the patient. This percentage ranges from 70 to 100% with a mean of 91% and a standard deviation of 3%. Moreover, one of the main advantage of the approach described in this paper is that all images could be used contrary to the inverse approach where the failure rate is about 20% on the same data set [28].

For the results exposed in this study, the pre-processing phase and the loading of all post-processed images take 4:52 minutes and 2:46 minutes, respectively. In the training process every generation of the 20 bats takes on average 6:35 minutes with a starting generation of 11:28 minutes, 1 Bat alone takes an average of 40.26 seconds. Finally, the complete stage of training and tuning of parameters takes a total of 1:55:12 hours for dataset 1.

VI. DISCUSSION

The context of this work is the development of novel medical device aiming to complement the current gold standard for bone status assessment, i.e., DXA. Even if DXA remains the current gold standard, it is limited by the difficulty to set a threshold in the aBMD distribution for osteoporosis diagnosis [5]. However, to this day, no alternative technique, with a fracture prediction ability significantly superior to DXA, has emerged.

The aim of this paper was to propose a new paradigm, exploring automatic classification tools, without the need of any underlying physical model. SVM approach was applied on ultrasonic guided wave spectrum images, obtained from a previous cross sectional study. In this previous study, inverse problem approach was tested and cortical porosity was found as discriminant as femoral aBMD after adjustment on age, BMI and cortisone intake. In this paper, 32 features have been extracted for each guided wave spectrum image. Some of these parameters showed AUC about 70 - 75%, similar to aBMD and Ct.Po (Tables 1 and 2). On the one hand, logistic regression associated with odd ratios and ROC curve, is of current use by clinicians. Its principle is based on weighted least squares algorithm allowing to fit the data with a linear regression, which may limit the performance if this assumption is not verified, or in case of large number of variables or if the variables are highly correlated. On the other hand, SVM

principle is based on a separation boundary, or hyperplane, in a multiple dimension space. These two methods have been often compared [56], [57], the advantages of tuned SVM depending on the complexity of the data. Even if accuracy, provided by SVM, and AUC, provided by logistic regression, are somehow similar, they correspond to different concepts [58], [59]. Logistic regression was used here as a reference method in a clinical context.

Using all 32 features without optimization, no significant improvement was observed, i.e., accuracy remained about 70 - 75% (Table 4). One of the main results of this paper is that, using BOA the accuracy significantly improved to about 90%, in this case larger than the aBMD accuracy (Table 4). Moreover, when regrouping images per patient, all patients are correctly classified. This result has to be mitigated by the fact that only 20% of the database was used as input data for the testing phase, even it has been randomly tested 20 times.

Moreover, the interest of the pre-processing step can be quantified in the following way: during the sampling phase, we tested the same environment without the pre-processing and obtain for the dataset 1 an accuracy of 86.84% lower than the accuracy of 92.31% obtained with the application of the pre-processing process. This result suggests that the pre-processing step and in particular the mask application effectively allows to retain the guided wave information, while removing the noise.

Indeed, these results have to be confirmed using other databases of guided wave spectrum images potentially obtained in different hospitals. Surely, a deeper analysis of the physical meaning and significance of the 32 features will be needed. In this paper, it can already be observed that the three ROIs present different behavior: ROI1 is discriminant without adjustment whereas ROI3 is discriminant after adjustment while ROI2 is almost never discriminant. These ROIs have been chosen considering physical arguments about guided waves: ROI1 is associated with $A0$ mode, guided mode of lowest phase velocity while ROI3 is associated with the modes of highest phase velocities and high dispersion branches corresponding to multiple paths between the two cortical layer boundaries [52]. This domain has been shown to be the less affected by the surrounded soft tissue corresponding to velocities close to the water, i.e., close to 1.5 mm.μ s^{-1}. The fact that ROI3 parameters are discriminant after age, BMI and cortisone adjustment could be of significant clinical interest if confirmed with other studies. It suggests that non-traumatic fractures may be linked with irregularities of the internal cortical boundaries, associated with trabecularisation and impaired bone remodeling [60].

Regarding future work, it is worth noting that more calculated features related to GLCM could be included, as well as different ROIs. Also, the number of generations and agents in the execution of metaheuristics will be increased for the adjustment of γ and C parameters. Also, as future work we will explore the automatic classification with different hybrid techniques [61]–[63] and the significance and physical interpretation of each feature. Finally, special attention will be given to achieving a reduction of false positives and false negatives generated by the model, looking forward to reducing the possibility of a misdiagnosis.

VII. CONCLUSION

In this work, a model was presented for the classification of patients with non-traumatic fractures and without non-traumatic fractures from guided wave spectrum images obtained with a Bi-Directional Axial Transmission (BDAT) device and a dynamic machine learning approach. This model consists of a Support Vector Machine (SVM), with parameter adjustment using a bio-inspired algorithm, which corresponds to Bat Algorithm Optimization (BOA). This exploratory study opens perspective towards a robust ultrasonic DXA alternative using automatic classification of guided wave spectrum images obtained with a BDAT device.

ABBREVIATIONS

aBMD:	areal Bone Mineral Density;
ACC:	Accuracy;
ASM:	Second Moment;
AUC:	Area Under the (ROC) Curve;
BOA:	Bat Algorithm Optimization;
BDAT:	Bi-Directional Axial Transmission;
BMI:	Body Mass Index;
CNN:	Convolutional Neural Networks;
Ct.Po:	cortical porosity;
Ct.Th:	cortical thickness;
DXA:	Dual-energy X-ray Absorptiometry;
GLCM:	Gray Level Concurrency Matrix;
KNN:	K-Nearest Neighbors;
LF:	Linear Functions;
MRI:	Magnetic Resonance Imaging;
MSE:	Mean Square Error;
ROC:	Receiver Operating Characteristic;
ROI:	Regions Of Interest;
SSIM:	Structural SIMilarity index;
SVM:	Support Vector Machine

ACKNOWLEDGMENT

The authors would like to acknowledge Azalée, the clinical team of Cochin hospital, in particular Sami Kolta, Karine Briot, Christian Roux. Finally, the authors would like to show their gratitude to Camila Alvarado for the invaluable support in the elaboration of the Figures.

AVAILABILITY OF DATA AND MATERIAL

Please contact the authors for data requests.

REFERENCES

[1] P. Sambrook and C. Cooper, "Osteoporosis," *Lancet*, vol. 367, no. 9527, pp. 2010–2018, 2006.

[2] E. M. Curtis, R. J. Moon, N. C. Harvey, and C. Cooper, "Reprint of: The impact of fragility fracture and approaches to osteoporosis risk assessment worldwide," *Int. J. Orthopaedic Trauma Nursing*, vol. 26, pp. 7–17, Aug. 2017.

[3] C. Cooper, G. Campion, and L. J. Melton, "Hip fractures in the elderly: A world-wide projection," *Osteoporosis Int.*, vol. 2, no. 6, pp. 285–289, Nov. 1992.
[4] J. A. Kanis, "The challenges of diagnosing osteoporosis and the limitations of currently available tools," *Clin. Diabetes Endocrinol.*, vol. 359, no. 9321, pp. 1929–1936, Jun. 2018.
[5] P. Choksi, K. J. Jepsen, and G. A. Clines, "The challenges of diagnosing osteoporosis and the limitations of currently available tools," *Clin. Diabetes Endocrinol.*, vol. 4, no. 1, p. 12, May 2018.
[6] P. Geusens, T. van Geel, K. Huntjens, S. van Helden, S. Bours, and J. van den Bergh, "Clinical fractures beyond low BMD," *Int. J. Clin. Rheumatol.*, vol. 6, no. 4, pp. 411–421, Aug. 2011.
[7] R. Kral, M. Osima, T. T. Borgen, R. Vestgaard, E. Richardsen, and Å. Bjørnerem, "Increased cortical porosity and reduced cortical thickness of the proximal femur are associated with nonvertebral fracture independent of Fracture Risk Assessment Tool and Garvan estimates in postmenopausal women," *PLoS ONE*, vol. 12, no. 9, Sep. 2017, Art. no. e0185363.
[8] S. Stagi, L. Cavalli, T. Cavalli, M. de Martino, and M. L. Brandi, "Peripheral quantitative computed tomography (pQCT) for the assessment of bone strength in most of bone affecting conditions in developmental age: A review," *Italian J. Pediatrics*, vol. 42, no. 1, pp. 88–107, Dec. 2016.
[9] K. K. Nishiyama, H. M. Macdonald, H. R. Buie, D. A. Hanley, and S. K. Boyd, "Postmenopausal women with osteopenia have higher cortical porosity and thinner cortices at the distal radius and tibia than women with normal aBMD: An *in vivo* HR-pQCT study," *J. Bone Mineral Res.*, vol. 25, no. 4, pp. 882–890, 2010.
[10] A. Ostertag, F. Peyrin, P. J. Gouttenoire, J. D. Laredo, M. C. DeVernejoul, M. C. Solal, and C. Chappard, "Multiscale and multimodality computed tomography for cortical bone analysis," *Phys. Med. Biol.*, vol. 61, no. 24, pp. 8553–8576, Dec. 2016.
[11] A. L. Hong, M. Ispiryan, M. V. Padalkar, B. C. Jones, A. S. Batzdorf, S. S. Shetye, N. Pleshko, and C. S. Rajapakse, "MRI-derived bone porosity index correlates to bone composition and mechanical stiffness," *Bone Rep.*, vol. 11, Dec. 2019, Art. no. 100213. [Online]. Available: http://www.sciencedirect.com/science/article/pii/S2352187219300191
[12] D. Hans and S. Baim, "Quantitative ultrasound (QUS) in the management of osteoporosis and assessment of fracture risk," *J. Clin. Densitometry*, vol. 20, no. 3, pp. 322–333, Jul. 2017.
[13] E. V. McCloskey, J. A. Kanis, A. Odén, N. C. Harvey, D. Bauer, J. González-Macias, D. Hans, S. Kaptoge, M. A. Krieg, T. Kwok, F. Marin, A. Moayyeri, E. Orwoll, C. Gluër, and H. Johansson, "Predictive ability of heel quantitative ultrasound for incident fractures: An individual-level meta-analysis," *Osteoporosis Int.*, vol. 26, no. 7, pp. 1979–1987, Jul. 2015.
[14] R. Barkmann, E. Kantorovich, C. Singal, D. Hans, H. K. Genant, M. Heller, and C.-C. Glüer, "A new method for quantitative ultrasound measurements at multiple skeletal sites: First results of precision and fracture discrimination," *J. Clin. Densitometry*, vol. 3, no. 1, pp. 1–7, 2000.
[15] M. Talmant, S. Kolta, C. Roux, D. Haguenauer, I. Vedel, B. Cassou, E. Bossy, and P. Laugier, "*In vivo* performance evaluation of bi-directional ultrasonic axial transmission for cortical bone assessment," *Ultrasound Med. Biol.*, vol. 35, no. 6, pp. 912–919, Jun. 2009.
[16] E. Biver, J. Pepe, A. de Sire, T. Chevalley, and S. Ferrari, "Associations between radius low-frequency axial ultrasound velocity and bone fragility in elderly men and women," *Osteoporosis Int.*, vol. 30, no. 2, pp. 411–421, Feb. 2019.
[17] P. Moilanen, M. Määttä, V. Kilappa, L. Xu, P. H. F. Nicholson, M. Alén, J. Timonen, T. Jämsä, and S. Cheng, "Discrimination of fractures by low-frequency axial transmission ultrasound in postmenopausal females," *Osteoporosis Int.*, vol. 24, no. 2, pp. 723–730, Feb. 2013.
[18] G. Adami, G. Arioli, G. Bianchi, M. L. Brandi, C. Caffarelli, L. Cianferotti, D. Gatti, G. Girasole, S. Gonnelli, M. Manfredini, M. Muratore, E. Quarta, and L. Quarta, "Radiofrequency echographic multi spectrometry for the prediction of incident fragility fractures: A 5-year follow-up study," *Bone*, vol. 134, May 2020, Art. no. 115297.
[19] J. P. Karjalainen, O. Riekkinen, and H. Kröger, "Pulse-echo ultrasound method for detection of post-menopausal women with osteoporotic BMD," *Osteoporosis Int.*, vol. 29, no. 5, pp. 1193–1199, May 2018.
[20] P. Moilanen, "Ultrasonic guided waves in bone," *IEEE Trans. Ultrason., Ferroelectr., Freq. Control*, vol. 55, no. 6, pp. 1277–1286, Jun. 2008.
[21] J. Foiret, J.-G. Minonzio, C. Chappard, M. Talmant, and P. Laugier, "Combined estimation of thickness and velocities using ultrasound guided waves: A pioneering study on *in vitro* cortical bone samples," *IEEE Trans. Ultrason., Ferroelectr., Freq. Control*, vol. 61, no. 9, pp. 1478–1488, Sep. 2014.
[22] M. Granke, Q. Grimal, A. Saïed, P. Nauleau, F. Peyrin, and P. Laugier, "Change in porosity is the major determinant of the variation of cortical bone elasticity at the millimeter scale in aged women," *Bone*, vol. 49, no. 5, pp. 1020–1026, Nov. 2011. [Online]. Available: http://www.sciencedirect.com/science/article/pii/S8756328211011458
[23] N. Bochud, Q. Vallet, Y. Bala, H. Follet, J.-G. Minonzio, and P. Laugier, "Genetic algorithms-based inversion of multimode guided waves for cortical bone characterization," *Phys. Med. Biol.*, vol. 61, no. 19, pp. 6953–6974, Oct. 2016.
[24] J. Schneider, D. Ramiandrisoa, G. Armbrecht, Z. Ritter, D. Felsenberg, K. Raum, and J.-G. Minonzio, "*In vivo* measurements of cortical thickness and porosity at the proximal third of the tibia using guided waves: Comparison with site-matched peripheral quantitative computed tomography and distal high-resolution peripheral quantitative computed tomography," *Ultrasound Med. Biol.*, vol. 45, no. 5, pp. 1234–1242, May 2019.
[25] K. Xu, D. Ta, D. Cassereau, B. Hu, W. Wang, P. Laugier, and J.-G. Minonzio, "Multichannel processing for dispersion curves extraction of ultrasonic axial-transmission signals: Comparisons and case studies," *J. Acoust. Soc. Amer.*, vol. 140, no. 3, pp. 1758–1770, Sep. 2016.
[26] G. Renaud, P. Kruizinga, D. Cassereau, and P. Laugier, "*In vivo* ultrasound imaging of the bone cortex," *Phys. Med. Biol.*, vol. 63, no. 12, Jun. 2018, Art. no. 125010.
[27] H. Nguyen Minh, J. Du, and K. Raum, "Estimation of thickness and speed of sound in cortical bone using multifocus pulse-echo ultrasound," *IEEE Trans. Ultrason., Ferroelectr., Freq. Control*, vol. 67, no. 3, pp. 568–579, Mar. 2020.
[28] J. Minonzio, N. Bochud, Q. Vallet, D. Ramiandrisoa, A. Etcheto, K. Briot, S. Kolta, C. Roux, and P. Laugier, "Ultrasound-based estimates of cortical bone thickness and porosity are associated with nontraumatic fractures in postmenopausal women: A pilot study," *J. Bone Mineral Res.*, vol. 34, no. 9, pp. 1585–1596, Sep. 2019.
[29] J.-G. Minonzio, N. Bochud, Q. Vallet, Y. Bala, D. Ramiandrisoa, H. Follet, D. Mitton, and P. Laugier, "Bone cortical thickness and porosity assessment using ultrasound guided waves: An ex vivo validation study," *Bone*, vol. 116, pp. 111–119, Nov. 2018.
[30] C. Cortes and V. Vapnik, "Support-vector networks," *Mach. Learn.*, vol. 20, no. 3, pp. 273–297, 1995.
[31] A. S. Lundervold and A. Lundervold, "An overview of deep learning in medical imaging focusing on MRI," *Zeitschrift für Medizinische Physik*, vol. 29, no. 2, pp. 102–127, May 2019.
[32] M. K. Abd-Ellah, A. I. Awad, A. A. M. Khalaf, and H. F. A. Hamed, "Two-phase multi-model automatic brain tumour diagnosis system from magnetic resonance images using convolutional neural networks," *EURASIP J. Image Video Process.*, vol. 2018, no. 1, p. 97, Sep. 2018.
[33] M.-J. Lian and C.-L. Huang, "Texture feature extraction of gray-level co-occurrence matrix for metastatic cancer cells using scanned laser pico-projection images," *Lasers Med. Sci.*, vol. 34, no. 7, pp. 1503–1508, Jul. 2018.
[34] I. Khatik, "A study of various bone fracture detection techniques," *Int. J. Eng. Comput. Sci.*, vol. 6, no. 5, pp. 21418–21423, Jun. 2017.
[35] S. W. Chung, S. S. Han, J. W. Lee, K.-S. Oh, N. R. Kim, J. P. Yoon, J. Y. Kim, S. H. Moon, J. Kwon, H.-J. Lee, Y.-M. Noh, and Y. Kim, "Automated detection and classification of the proximal humerus fracture by using deep learning algorithm," *Acta Orthopaedica*, vol. 89, no. 4, pp. 468–473, Mar. 2018.
[36] W. W. Myint, K. S. Tun, and H. M. Tun, "Analysis on leg bone fracture detection and classification using X-ray images," *Mach. Learn. Res.*, vol. 3, no. 3, pp. 49–59, 2018.
[37] M. Correa, M. Zimic, F. Barrientos, R. Barrientos, A. Román-Gonzalez, M. J. Pajuelo, C. Anticona, H. Mayta, A. Alva, L. Solis-Vasquez, D. A. Figueroa, M. A. Chavez, R. Lavarello, B. Castañeda, V. A. Paz-Soldán, W. Checkley, R. H. Gilman, and R. Oberhelman, "Automatic classification of pediatric pneumonia based on lung ultrasound pattern recognition," *PLoS ONE*, vol. 13, no. 12, Dec. 2018, Art. no. e0206410.
[38] N. Baka, S. Leenstra, and T. van Walsum, "Random forest-based bone segmentation in ultrasound," *Ultrasound Med. Biol.*, vol. 43, no. 10, pp. 2426–2437, Oct. 2017.
[39] M. Villa, G. Dardenne, M. Nasan, H. Letissier, C. Hamitouche, and E. Stindel, "FCN-based approach for the automatic segmentation of bone surfaces in ultrasound images," *Int. J. Comput. Assist. Radiol. Surgery*, vol. 13, no. 11, pp. 1707–1716, Nov. 2018.

[40] P. Mielnik, M. Fojcik, J. Segen, and M. Kulbacki, "A novel method of synovitis stratification in ultrasound using machine learning algorithms: Results from clinical validation of the MEDUSA project," *Ultrasound Med. Biol.*, vol. 44, no. 2, pp. 489–494, Feb. 2018.
[41] M. Denis, L. Wan, M. Fatemi, and A. Alizad, "Ultrasound characterization of bone demineralization using a support vector machine," *Ultrasound Med. Biol.*, vol. 44, no. 3, pp. 714–725, Mar. 2018.
[42] F. Vogl, B. Friesenbichler, L. Hüsken, I. A. Kramers-de Quervain, and W. R. Taylor, "Can low-frequency guided waves at the tibia paired with machine learning differentiate between healthy and osteopenic/osteoporotic subjects? A pilot study," *Ultrasonics*, vol. 94, pp. 109–116, Apr. 2019.
[43] K. Mohanty, O. Yousefian, Y. Karbalaeisadegh, M. Ulrich, Q. Grimal, and M. Müller, "Artificial neural network to estimate micro-architectural properties of cortical bone using ultrasonic attenuation: A 2-D numerical study," *Comput. Biol. Med.*, vol. 114, Nov. 2019, Art. no. 103457.
[44] Y. Li, K. Xu, Y. Li, B. Hu, J. Zhang, L. H. Le, and D. Ta, "Multichannel crossed convolutional neural network for combined estimation of cortical thickness and bulk velocities using ultrasonic guided waves: A simulation study," in *Proc. IEEE Int. Ultrason. Symp. (IUS)*, Glasgow, U.K., Oct. 2019, pp. 2412–2415.
[45] K. S. Alguri, J. Melville, and J. B. Harley, "Baseline-free guided wave damage detection with surrogate data and dictionary learning," *J. Acoust. Soc. Amer.*, vol. 143, no. 6, pp. 3807–3818, Jun. 2018.
[46] R. Miorelli, A. Kulakovskyi, O. Mesnil, and O. d'Almeida, "Automatic defect localization and characterization through machine learning based inversion for guided wave imaging in SHM," in *Proc. AIP Conf.* vol. 2102, 2019, Art. no. 050005.
[47] X.-S. Yang, *A New Metaheuristic Bat-Inspired Algorithm*. Berlin, Germany: Springer, 2010, pp. 65–74.
[48] E. Bossy, M. Talmant, M. Defontaine, F. Patat, and P. Laugier, "Bidirectional axial transmission can improve accuracy and precision of ultrasonic velocity measurement in cortical bone: A validation on test materials," *IEEE Trans. Ultrason., Ferroelectr., Freq. Control*, vol. 51, no. 1, pp. 71–79, Jan. 2004.
[49] J.-G. Minonzio, M. Talmant, and P. Laugier, "Guided wave phase velocity measurement using multi-emitter and multi-receiver arrays in the axial transmission configuration," *J. Acoust. Soc. Amer.*, vol. 127, no. 5, pp. 2913–2919, May 2010.
[50] J.-G. Minonzio, J. Foiret, M. Talmant, and P. Laugier, "Impact of attenuation on guided mode wavenumber measurement in axial transmission on bone mimicking plates," *J. Acoust. Soc. Amer.*, vol. 130, no. 6, pp. 3574–3582, Dec. 2011.
[51] L. Moreau, J.-G. Minonzio, M. Talmant, and P. Laugier, "Measuring the wavenumber of guided modes in waveguides with linearly varying thickness," *J. Acoust. Soc. Amer.*, vol. 135, no. 5, pp. 2614–2624, May 2014.
[52] N. Bochud, Q. Vallet, J.-G. Minonzio, and P. Laugier, "Predicting bone strength with ultrasonic guided waves," *Sci. Rep.*, vol. 7, no. 1, p. 43628, May 2017.
[53] Z. Wang, A. C. Bovik, H. R. Sheikh, and E. P. Simoncelli, "Image quality assessment: From error visibility to structural similarity," *IEEE Trans. Image Process.*, vol. 13, no. 4, pp. 600–612, Apr. 2004.
[54] R. M. Haralick, K. Shanmugam, and I. Dinstein, "Textural features for image classification," *IEEE Trans. Syst., Man, Cybern.*, vol. SMC-3, no. 6, pp. 610–621, Nov. 1973.
[55] N. Nachar, "The mann-whitney U: A test for assessing whether two independent samples come from the same distribution," *Tuts. Quant. Methods for Psychol.*, vol. 4, no. 1, pp. 13–20, Mar. 2008.
[56] T. Verplancke, S. Van Looy, D. Benoit, S. Vansteelandt, P. Depuydt, F. De Turck, and J. Decruyenaere, "Support vector machine versus logistic regression modeling for prediction of hospital mortality in critically ill patients with haematological malignancies," *BMC Med. Informat. Decis. Making*, vol. 8, no. 1, p. 56, Dec. 2008.
[57] E. Ing, W. Su, M. Schonlau, and N. Torun, "Support vector machines and logistic regression to predict temporal artery biopsy outcomes," *Can. J. Ophthalmol.*, vol. 54, no. 1, pp. 116–118, Feb. 2019.
[58] A. B. Musa, "Comparative study on classification performance between support vector machine and logistic regression," *Int. J. Mach. Learn. Cybern.*, vol. 4, no. 1, pp. 13–24, Feb. 2013.
[59] H. Rashidi, N. Tran, E. Betts, L. Howell, and R. Green, "Artificial intelligence and machine learning in pathology: The present landscape of supervised methods," *Acad. Pathol.*, vol. 6, pp. 1–16, Sep. 2019.
[60] G. Osterhoff, E. F. Morgan, S. J. Shefelbine, L. Karim, L. M. McNamara, and P. Augat, "Bone mechanical properties and changes with osteoporosis," *Injury*, vol. 47, pp. S11–S20, Jun. 2016.
[61] P. Tiwari and M. Melucci, "Towards a quantum-inspired binary classifier," *IEEE Access*, vol. 7, pp. 42354–42372, 2019.
[62] R. Munoz, R. Olivares, C. Taramasco, R. Villarroel, R. Soto, T. S. Barcelos, E. Merino, and M. F. Alonso-Sánchez, "Using black hole algorithm to improve EEG-based emotion recognition," *Comput. Intell. Neurosci.*, vol. 2018, pp. 1–21, Jun. 2018.
[63] R. Munoz, R. Olivares, C. Taramasco, R. Villarroel, R. Soto, M. F. Alonso-Sánchez, E. Merino, and V. H. C. de Albuquerque, "A new EEG software that supports emotion recognition by using an autonomous approach," *Neural Comput. Appl.*, vol. 32, no. 15, pp. 11111–11127, Dec. 2018.

JEAN-GABRIEL MINONZIO was born in Dijon, France, in 1978. He received the B.S. degree in engineering physics from the Ecole Supérieure de Physique et de Chimie Industrielles de la Ville de Paris, Paris, France, in 2003, and the M.S. and Ph.D. degrees in physical acoustics from University Denis Diderot, Paris, in 2003 and 2006, respectively. He has been involved in elastic guided waves in cortical bone with the Laboratoire d'Imagerie Biomédicale, Sorbonne Université, Paris. He has also been involved in the measurement of guided waves in cortical bones for about ten years. He is currently detached from French CNRS and is currently working as a Professor with the School of Informatics Engineering, Universidad de Valparaíso. His main research areas include array signal processing, wave propagation modeling, and inverse problem in applied ultrasound. He is a part of the Board of The International Bone Ultrasound Society (BoneUS).

BRYAN CATALDO is currently pursuing the degree in computer engineering with the Potificia Universidad Católica de Valparaíso. His thesis is about the automatic classifying of patients with non-traumatic fractures based on ultrasonic guided wave spectrum image using a dynamic machine learning approach. His research interests are focused on machine learning and software development.

RODRIGO OLIVARES (Member, IEEE) received the M.Sc. and Ph.D. degrees in computer science. He is currently an Assistant Professor with the School of Informatics Engineering, Universidad de Valparaíso. His main areas of research interest include reactive and self-adaptive metaheuristics, global optimization, and machine learning. He has authored several contributions in relevant scientific journals and prestigious conferences about optimization and artificial intelligence swarm intelligence algorithms.

DONATIEN RAMIANDRISOA received the B.S. degree in engineering physics from the Ecole Supérieure de Physique et de Chimie Industrielles de la Ville de Paris, Paris, France, in 2010, and the M.S. and Ph.D. degrees in physical chemistry from the University Pierre et Marie Curie, Paris, in 2010 and 2014, respectively. He is currently working as a Software Development Engineer with Bleu Solid.

RICARDO SOTO received the Ph.D. degree in computer science from the University of Nantes, France, in 2009. He is currently a Full Professor and the Head of the Computer Science Department, Pontifical Catholic University of Valparaíso, Chile. His main areas of research interest include metaheuristics, global optimization, and autonomous search. In this context, he has published more than 200 scientific papers in different international conferences and journals, some of them top-ranked in computer science, operational research, and artificial intelligence. Most of these papers are based on the resolution of real-world and academic optimization problems related to industry, manufacturing, rostering, and seaports.

BRODERICK CRAWFORD (Member, IEEE) received the Ph.D. degree in computer science from the Universidad Técnica Federico Santa María of Valparaíso, Chile, in 2011. He is currently a Full Professor with the Computer Science Department, Pontifical Catholic University of Valparaíso, Chile. His main areas of research interest include combinatorial optimization, metaheuristics, global optimization, and autonomous search. In this context, he has published over 300 scientific papers in different international conferences and journals, some of them are top-ranked in computer science, operational research, and artificial intelligence. Most of these papers are based on the resolution of benchmark and real-world optimization problems.

VICTOR HUGO C. DE ALBUQUERQUE (Senior Member, IEEE) graduated in mechatronics engineering from the Federal Center of Technological Education of Ceará, the M.Sc. degree in teleinformatics engineering from the Federal University of Ceará, and the Ph.D. degree in mechanical engineering from the Federal University of Paraíba. He is a specialist, mainly, in IoT, machine/deep learning, pattern recognition, and robotics.

ROBERTO MUNOZ (Member, IEEE) received the master's degrees in computer engineering, engineering science, and education, and the Ph.D. degree in computer engineering. He is currently the Head of the School of Informatics Engineering, Universidad de Valparaíso, Chile. He has authored over 90 scientific papers and is a TPC member in refereed international conferences and highly reputed journals. His research interests include computers and education, multimodal learning analytics, human-computer interaction, and health informatics.